Peek into the world of materials using thermopower and XAFS as investigative probes

Preeti A. Bhobe*

Discipline of Physics, Indian Institute of Technology Indore, Simrol, Indore 453 552, India

Over the last few decades, there has been growing interest for developing technologies aimed at providing cleaner and more sustainable energy sources. Great efforts are directed towards synthesis of newer functional materials and tailoring the existing ones with an aim to optimize their usability. As materials are being developed with various complexities in their physical properties and forms like single crystals, thin-films, nanostructure and composites, measurement of their basic physical properties is also getting equally challenging. This review deals with a brief summary of our efforts in developing the basic understanding of some functional materials, using experimental tools that are best known to us, viz. measurement of Seebeck coefficient and X-ray absorption fine structure spectroscopy (XAFS). In particular, we discuss the results of our investigation of magnetic shape memory alloy Ni_2MnGa and multiferroic $CdCr_2Se_4$.

Keywords: Magnetic shape memory alloys, XAFS, thermopower measurements, spin–phonon coupling, magnetic semiconductors.

Introduction

THE present age research in materials science is largely focussed around providing alternative technologies aimed at cleaner and more sustainable energy sources. Hence the mention of thermoelectric power in the perspective of contemporary research generally implies new schemes for materials synthesis and device fabrication with enhanced performance. This article, however, focusses on thermopower and XAFS measurements as an investigative tool, used for understanding material properties, not limited to thermoelectrics.

What is thermoelectric power?

In most simple terms, thermoelectric power or thermoelectricity is all about generating electrical power from heat, using a solid-state device without combustion or moving parts. It is an effect that involves interplay between electrical and thermal properties of a material

with electrons acting as the active fluid. The two primary physical phenomena that are at play in thermoelectrics are the Seebeck effect and the Peltier effect.

Discovered in 1821 by T. J. Seebeck and hence named after him, this effect describes how a temperature gradient (ΔT) across a conductor leads to electric charge flow, causing a measureable potential gradient (V) across it. Thus, $V = S\Delta T$, where S is the Seebeck coefficient. The opposite effect, i.e. generation of temperature gradient upon passage of electric current (I) through a conductor was discovered by J. Peltier. The expression for heat absorbed/emitted being, $Q = \pi I$, where π is the Peltier coefficient. It was not until 1855, when W. Thomson (Lord Kelvin), using thermodynamics laws, showed that the Seebeck and Peltier effects are basically inter-linked. He also pointed out the need for the third effect to be considered, which is reversible heating or cooling when there is both a flow of electric current and a temperature gradient.

Thus was the birth of a concept – a type of heat engine that could be used either as a device for generating electricity from heat or, alternatively, as a heat pump or refrigerator. However, upon practical considerations, it was realized that supplementary to the thermoelectric effect are the unfavourable phenomena of Joule heating and thermal conduction. This makes the thermoelectric generators inefficient heat engines compared to its mechanical counterpart[1].

In 1911, Altenkirch[2] worked on this issue and showed that the performance of a thermocouple could be improved by increasing the magnitude of the differential Seebeck coefficient – which in turn could be improved by raising the electrical conductivity and lowering the thermal conductivity of the materials used in the two arms of a thermocouple. Unfortunately, those were early days of Solid State Physics as we know it today and hence the idea of manipulating materials at electronic band structure level had not developed then. Serious efforts in the direction of practical application only started during the late 1950s with the advent of thermoelectric power generators for spacecrafts by NASA (USA). Since then began the search for a perfect combination of materials that would form an efficient thermoelectric generator. Presently, applicability of such devices however is restricted to small-scale applications like thermocouple temperature sensors and cooling in laser diodes or wine cellars.

*e-mail: pbhobe@iiti.ac.in

From the viewpoint of basic science, measurement of Seebeck coefficient (thermopower or TEP) of a material provides an insight into its electronic structure, and type of carriers, whether holes or electrons. Being a transport property that involves entropy change, it also carries significant information about processes like phase transitions that may take place in a solid. Unlike electrical resistivity, thermopower measurement does not involve errors in the measured quantity relating to sample dimensions. Practically, thermopower is given by a measurement of the ratio of sample voltage to the temperature gradient along the sample

$$S = \frac{\Delta V}{\Delta T} = \frac{(V_h - V_c)}{(T_h - T_c)},$$

where the symbols have their usual meaning and the subscripts h and c refer to hot and cold respectively. In general, thermopower, like any other thermal property can show distinct variation with the anisotropy in the crystallographic orientations of the sample, so does electrical resistivity. This aspect can be considered by carrying out measurements along differently oriented pieces of the same sample.

Measurement of S can be essentially carried out using two techniques. First is, to fix the sample temperature to a desired value T and develop a small temperature gradient ΔT across it and measure the sample voltage as a function of a gradient across the sample. The slope of such a line yields S. This is a simple technique but slow, especially under the circumstances where one wants to measure S as a function of temperature. The other technique is to apply a small 'fixed' temperature gradient across the sample and slowly vary the overall temperature T. At each temperature of interest, several voltage measurements are made and S is calculated from the above given relationship. In this technique, it needs to be periodically ensured that ΔV is linear in ΔT and $\Delta V \to 0$ at

$\Delta T \to 0$, else such measurement is susceptible to a DC offset voltage error.

Whichever be the technique used, thermopower measurements only seem conceptually simple. Thermal contact errors must be minimized else heat will flow through other paths having higher thermal conductivity. A test of known standards should be carried out from time to time. If there is a significant time lag between sample voltage and thermocouple voltage, it implies that there is a problem with thermal anchoring of the thermocouple and/or the sample. While recording the sample voltage, one should ensure that the sample is electrically isolated from the rest of the sample stage assembly. The measured S value includes both the sample and lead (normally, Au Cu) contribution. So the lead contribution must be subtracted from each measurement.

What is XAFS?

XAFS or X-ray absorption fine structure spectroscopy is a technique employed to study the chemical environment of the atoms in a crystal. In what follows, XAFS has been explained using a more heuristic approach. For more information on XAFS the reader may explore refs 3–5. When a high energy X-ray photon is incident on a material, a core level electron from the constituent atom is emitted if the incident energy of the photons exceeds it's binding energy. This causes a sharp dip in the transmitted intensity which is called 'absorption edge'. The outgoing photo-electron can be thought of as a spherical wave expanding in all directions (see Figure 1 for the cartoon). When such a wave reaches the neighbouring atoms, it will be partially back-scattered. The back-scattered wave interferes with the outgoing electron wave causing a constructive or a destructive interference. The net effect is the modulation of transmitted X-rays much away from the absorption edge energy. The interference pattern depends mainly on the number, nature and distance of the surrounding atoms from the absorbing atom.

Hence, XAFS provides a relatively simple way to determine the local crystal structure around the atom of interest contained in a solid. This information is not accessible by the common X-ray diffraction technique which relies entirely on the long range crystalline order of the samples under study. The probability that X-rays will be absorbed by the particular atom constituting the sample depends on the absorption coefficient μ, absorber thickness t, and given by Beer's law as, $I = I_0 \exp(-\mu t)$ where I_0 and I are the X-ray intensities incident on, and transmitted through, the sample absorber respectively. Plainly stated, XAFS measures the energy dependence of μ at and above the binding energy of the core level of the atom under investigation. As the incident X-ray energy is tuned to the range of the absorption edge of the element of interest, XAFS is known to be an element specific technique.
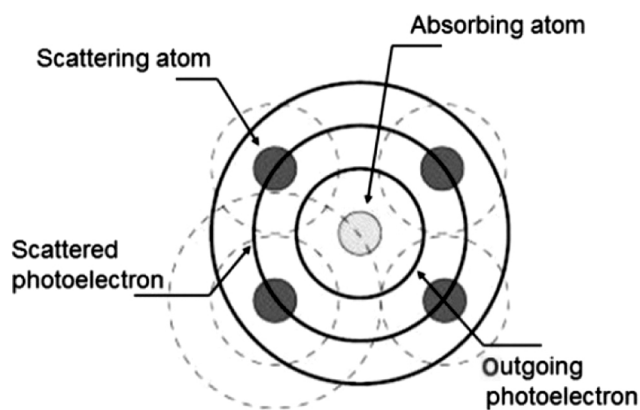

Figure 1. Cartoon demonstrating the interference between the emitted and backscattered photoelectron that gives rise to fine structure in absorption spectrum.

XAFS can be measured either in transmission or fluorescence geometry. The energy dependence of the absorption coefficient for transmission mode can be written as

$$\mu(E) = \ln(I_0/I).$$

And for fluorescence mode,

$$\mu(E) \propto I_f/I$$

where I_0 refers to the incident intensity and I_f is the intensity of the fluorescence line.

The fine structure function $\chi(E)$ is defined as

$$\chi(E) = \frac{\mu(E) - \mu_0(E)}{\Delta\mu_0(E)},$$

where $\mu(E)$ is the measured absorption coefficient, $\mu_0(E)$ a smooth background function representing the absorption of an isolated atom and $\Delta\mu_0(E)$ is the measured jump in absorption $\mu(E)$ at the threshold energy E_0 (Figure 2).

The X-ray energy is then converted to k, the wave number of the photo-electron, which has dimensions of 1/distance. The primary quantity for XAFS is then $\chi(k)$, the oscillations as a function of photo-electron w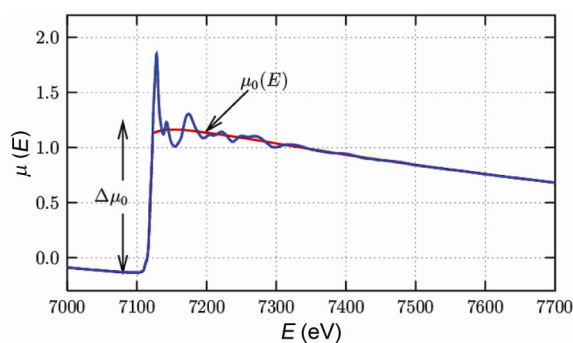ave number, apparent in Figure 3. Different frequencies present in these oscillations of $\chi(k)$ can be separated by taking a Fourier transform to correspond to $\chi(R)$, which is different near neighbour coordination shells (Figure 4) that has to be modeled according to the XAFS equation, $\chi(k)$ as

$$\sum_j \left[\frac{N_j S_0^2 e^{-2k^2\sigma_j^2} e^{-2R_j/\lambda(k)} f_j(k)}{kR^2} \sin[2kR_j + \delta_j(k)] \right],$$

where $f(k)$ and $\delta(k)$ are scattering properties of the atoms neighbouring the excited atom, N the number of neighbouring atoms present at distance R and σ^2 is the mean square disorder in the bond distance.

Figure 4. Magnitude and real component of the Fourier transformed XAFS spectrum showing contributions of various coordination shells around the absorbing atom.

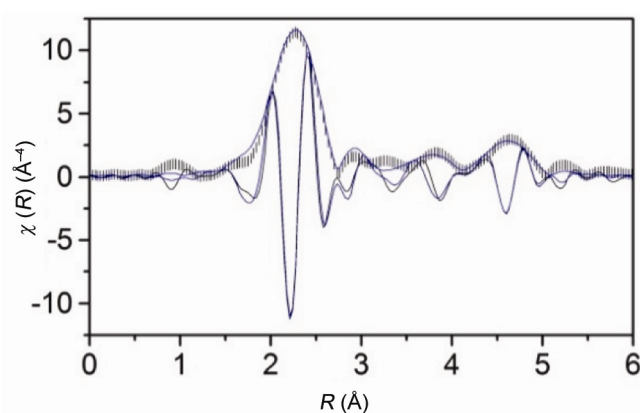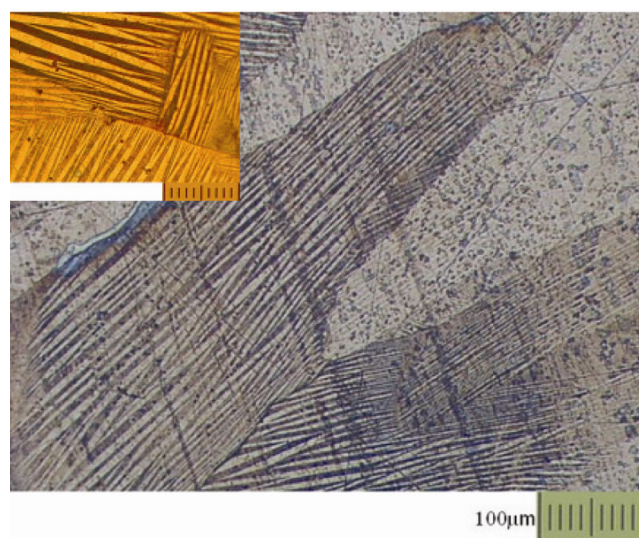**Figure 2.** The as-recorded XAFS spectrum. Data here pertains to the Fe K-edge absorption.
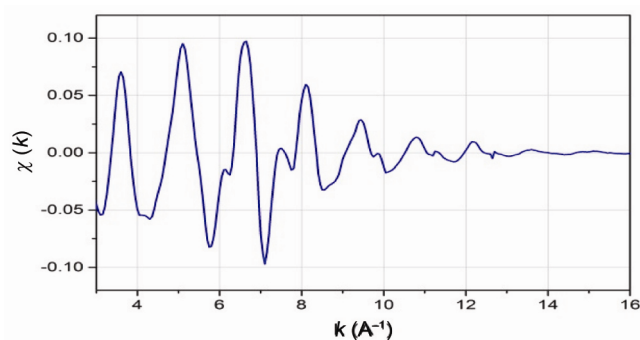
Figure 3. XAFS function $\chi(k)$, extracted from raw data shown previously in Figure 2.

Figure 5. Image of a sample of Ni–Mn–Ga as seen under an optical microscope. The modulated and the flat morphologies indicate the martensitic and cubic regions respectively, of a sample undergoing martensitic transformation. The inset shows another such sample where the transformation to martensitic phase is complete. © IOP Publishing. Reproduced with permission from ref. 7. All rights reserved.

The XAFS equation allows us to determine N, R, and σ^2 knowing the scattering amplitude $f(k)$ and the phase-shift $\delta(k)$. Furthermore, since these scattering factors depend on the Z-atomic number of the neighbouring atoms, XAFS is also sensitive to the atomic species of neighbouring atoms.

Ni–Mn–Ga shape memory alloys

Here, we present the study of local structural and thermopower aspects of the shape memory alloy (SMA), $Ni_{2+x}Mn_{1-x}Ga$ (refs 6–8). The outcome of such investigation presents new evidence for the crucial hybridization component that influences and leads to structural transitions in Ni–Mn based SMA. The inferences drawn from this work have been found to be robust and validated through experiments like photoemission spectroscopy by others[9,10], and in other SMA like Ni–Mn–In and Ni–Mn–Sn series by us[11–13]; here we present the case study of Ni–Mn–Ga series alone.

SMAs are materials that exhibit the unique property of remembering its shape prior to any deformation and can recover permanent strains when heated above a certain temperature. The key characteristic for the shape memory effect is the martensitic transformation that takes place with change in temperature. Martensitic transformations are first-order, diffusionless, solid-solid phase transformation taking place upon cooling below a characteristic temperature T_M from a high symmetry initial phase to a low-symmetry structure. Ni–Mn–Ga SMA gathered a lot of research interest because the martensitic transition takes place in ferromagnetic state. Therefore, in addition to pressure and temperature, magnetic field can also be used to control the shape memory effect. This is significant in the development of 'smart materials' as the magnetic response is much quicker than temperature response.

The broad class of intermetallic compositions to which Ni–Mn–Ga belongs, is represented by the general formula X_2YZ and known as 'Heusler alloys'. This class of materials is remarkable in that, besides SMA, there are compositions which exhibit interesting physical properties like half-metallicity, spin gapless semiconductors, heavy Fermion systems, superconductivity and topological insulators.

Background

Ni_2MnGa orders ferromagnetically at $T_C = 370$ K and the martensitic phase transition takes place at $T_M \sim 220$ K from the cubic L2$_1$ structure to a modulated tetragonal state at low temperature[14–16]. The total saturation moment of $\sim 4~\mu_B$, is mainly localized at Mn with very small contribution from rest of the atoms. Ferromagnetism is essentially of the *RKKY* type wherein there is an indirect Mn–Mn interaction mediated via conduction electrons provided by Ni (ref. 17). The low temperature crystal structure of the martensite is a periodic stacking sequence of the $\{110\}_p$ planes along the $\langle 1\bar{1}0 \rangle_p$ direction of the initial cubic system with modulations having crystal periodicity (Figure 5) like five-layered, seven-layered or non-modulated tetragonal structure[18].

Calculations of the electronic density of states (DOS) attribute the stability of low temperature structure to a dip in the minority-spin DOS at the Fermi level, related to the formation of hybrid states of Ni d and Ga p minority-spin orbitals[19].

After systematic preparation of $Ni_{2+x}Mn_{1-x}Ga$ by arc-melting and characterization by powder X-ray diffraction (XRD), scanning electron microscopy (SEM), optical microscopy, four-probe resistivity, a.c. magnetic susceptibility and magnetization, we recorded the variation in thermoelectric power (TEP) with temperature to investigate the changes in the density of states at the Fermi level occurring upon structural transformation. These studies were followed by focussed XAFS investigation of changes in local structure across the martensitic transformation.

Before we discuss the results, it is imperative to mention how the combination of TEP and XAFS is an ideal combination in the study of Ni–Mn–Ga alloys. Thermopower is one of the most sensitive indicators of changes in hybridization within a solid. As will be shown later in the text, TEP is proportional to the carrier density and the carrier mobility. Any change in the nature of hybridization primarily alters the carrier density, and the structural changes alter the carrier mobility. XAFS is an ideal technique to pick up such small changes in the local structure occurring within a unit cell, towards which the popular X-ray diffraction profiling is quite insensitive. Besides, Ni–Mn–Ga alloys undergo martensitic transitions and form modulated crystal structures giving rise to large grain boundaries that contribute heavily towards scattering of charge carriers. This scattering contribution masks the subtle signs of changing hybridization in an electrical resistivity measurement.

Results and discussion

Increasing Ni content in the series $Ni_{2+x}Mn_{1-x}Ga$, raises its T_M and lowers its T_C until they coincide at $x = 0.19$, as depicted in the adjoining Figure 6. There is a systematic increase in the electron per atom (e/a) ratio with Ni (3d^8) replacing Mn (3d^5) atoms. Thus this series provides an opportunity to span the transformation from austenitic to martensitic region by simply varying the Ni to Mn ratio and carrying out measurements at room temperature. TEP measurements were carried out using the home-built set-up in the temperature range 100 K to 350 K. The data was recorded while warming. The voltage difference ΔV

developed across the sample due to the temperature difference ΔT was measured at each desired temperature T. The sample was placed between two highly polished copper plates. The overall temperature of the system was
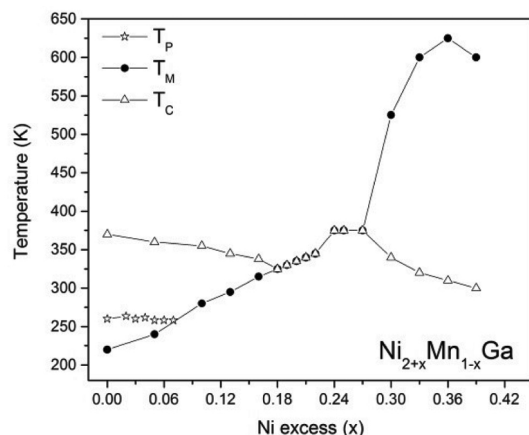

Figure 6. Phase diagram of Ni concentration versus temperature $Ni_{2+x}Mn_{1-x}Ga$ compositions depicting various phase transition temperatures.
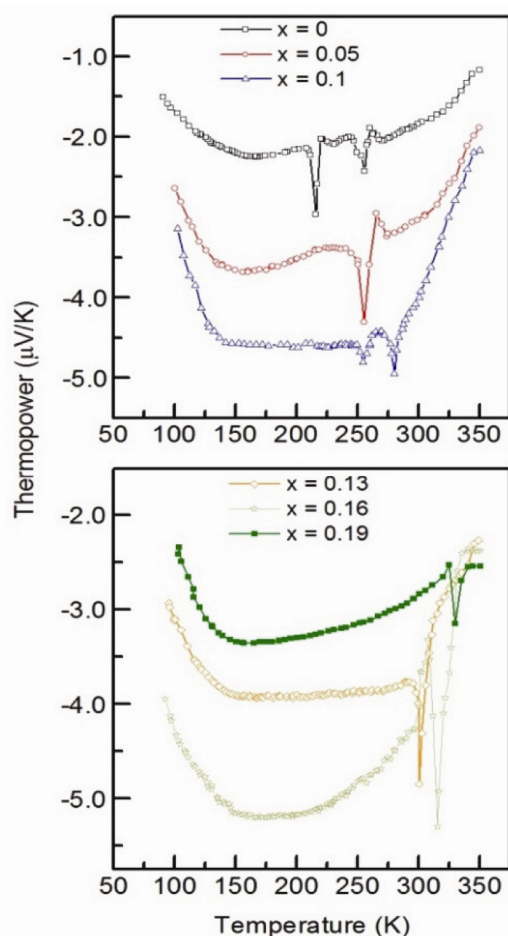

Figure 7. Temperature dependence of TEP measured for different compositions of the $Ni_{2+x}Mn_{1-x}Ga$ series. The data is presented in two panels to maintain clarity of the plots.

raised using two heaters attached to these copper plates and monitored using a platinum resistance thermometer. A copper-constantan thermocouple operating in the differential mode was employed to monitor the temperature gradient across the sample. This type of arrangement is termed as the 'differential method' of TEP measurement.

Temperature-dependent TEP profiles for $Ni_{2+x}Mn_{1-x}Ga$ compositions are presented in Figure 7. Transformation from cubic to martensitic phase being a first order change, it accompanies a change in the free energy. Accordingly, distinct dip-like feature seen in the TEP measurements is associated with T_M, while change in slope of TEP is observed near T_C. Some compositions also exhibit features ascribed to pre-martensitic and inter-martensitic transitions[20], the signatures associated with such transitions are also seen as an additional dip in the measured thermopower. Note that for composition with $x = 0.13$, the martensitic and magnetic transition take place within a close temperature range, just above room temperature. Hence large changes in TEP in narrow temperature interval are to be expected. Besides the signatures associated with increasing e/a, and those ascribed to a typical ferromagnetic metal (like TEP minima), we observe almost constant value of TEP over a wide range in temperature in the martensitic phase. This change occurs as a result of nesting vectors formed due to differently modulated crystal structures in the martensitic phase causing weak localization of conduction electrons, as described earlier[6–7].

The highlight of TEP measurements in Ni–Mn–Ga is the slope of TEP that changes quite sharply in going from Ni_2MnGa to $Ni_{2.19}Mn_{0.81}Ga$. This is clearer from Figure 8, where the derivative of TEP shows an inflection point that shifts from 0.86 to 0.94 of T/T_M with Ni content changing from 0 to 0.19. Such change implies increase in the DOS at Fermi level.
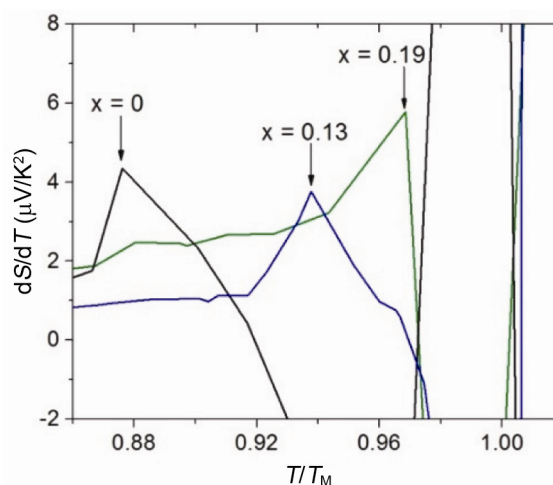

Figure 8. Derivative of thermopower versus temperature, normalized to T_M, for $Ni_{2+x}Mn_{1-x}Ga$ series. Only few representative compositions have been displayed here to maintain the clarity of the plots. © IOP Publishing. Reproduced with permission from ref. 7. All rights reserved.

To understand this, consider the simple semi-classical result for thermal diffusion only strictly valid in the case of metals and highly degenerate semiconductors. The expression for TEP in such scenario can be approximated to

$$S = -\frac{1}{e\sigma T}\int (\varepsilon - \mu)\frac{\partial f_0}{\partial \varepsilon}\sigma(\varepsilon)\mathrm{d}\varepsilon,$$

where f_0 is the Fermi–Dirac distribution function, μ is the chemical potential and σ the conductivity. The conductivity for a metallic system is directly proportional to DOS. Hence an increase of the electronic DOS near the Fermi level would result in enhancement of the thermopower. If a model for the DOS near Fermi level is assumed consisting of a peak, the observed TEP can be accounted for by such a peak shifting closer to the Fermi edge with rising Ni content. A sharply rising DOS implies the increased hybridization between certain atoms causing shift of bands at the Fermi-level.

XAFS measurements of Ni–Mn–Ga alloys help us to identify this hybridization of bands in an indirect way. Changing local crystal structure of the $Ni_{2+x}Mn_{1-x}Ga$ was traced by recording XAFS at Mn and Ga K-edges. Samples with $0 < x < 0.13$ of Ni content have cubic structure at room temperature as the T_M for these samples is below 300 K. However, for $x \sim 0.13$ and above, the samples are 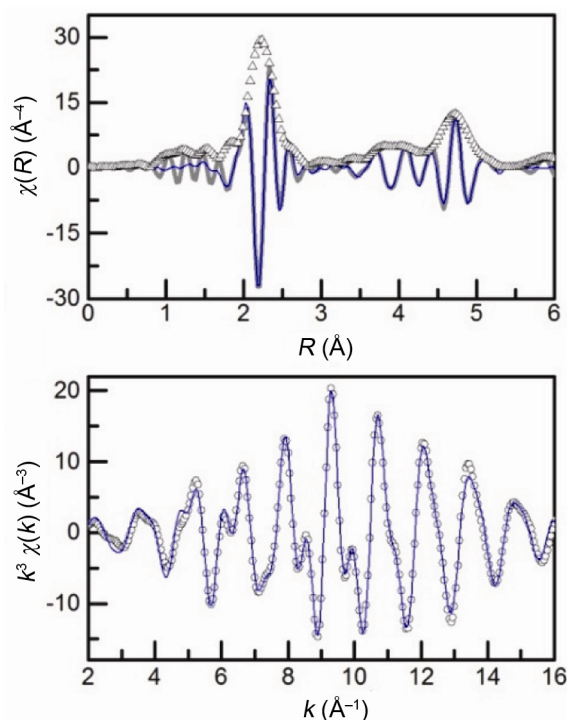already in the tetragonal phase with T_M above room temperature. Keeping this in view, XAFS spectra were fitted using appropriate structural models. The fitting process was described earlier[8,11]. The magnitude and real component of FT of XAFS spectra in R-space and real component of FT in the back transformed k-space for Mn K-edge data obtained for the parent composition of Ni_2MnGa is shown in Figure 9.

The findings from XAFS analyses[8] can be summarized in three major points: (i) higher values of σ^2 for Ga K-edge spectra in comparison to Mn K-edge in the martensitic phase of samples, (ii) different bond distances for Ga–Mn correlation when viewed from Ga edge and Mn edge; and (iii) Mn–Ni bond is larger by 0.016 Å as compared to Ga–Ni bond in the martensitic phase.

Higher values of σ^2 in other words, mean a distribution of Mn–Ga bond-lengths, and since this observation comes from the analysis of Ga data, it is the Mn atoms that move more freely. This is further corroborated by difference in the bond-lengths obtained for the same pair of atoms (i.e. Ga–Mn) from Ga XAFS and Mn XAFS. Further, there is a notable difference in the Mn–Ni and Ga–Ni bond-lengths. Figure 10 shows crystal structure schematic that makes it easier to interpret these results. It is seen that Ni atoms reside at the centre of the Mn and Ga tetrahedra. Ideally, for a cubic system Ni should have been equi-distant from both, Mn and Ga. Shorter Ga–Ni bonds obtained from XAFS indicate strong hybridization over Mn–Ni correlation. This implies sizable distortion of the Ga tetrahedron allowing more space for the movement of Mn, which moves with higher amplitude of displacement. Such a Ni–Ga hybridization has also been anticipated theoretically[18], where electronic band structure calculations yield energetically favourable hybrid states formed by Ga and Ni giving rise to a peak in the spin-down electronic density of states at the Fermi level. Also, observed TEP results compliment the XAFS analysis.

In general, the present study is a direct experimental evidence for X–Z hybridization in X_2YZ Heusler alloys that cause re-distribution of electrons and band
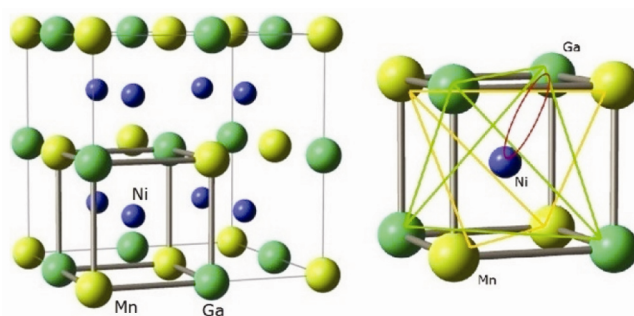

Figure 9. A representative fit of the FT components of fitted XAFS spectra in R space and back transformed k space for Ni_2MnGa. The fitting to the data are shown as coloured lines.

Figure 10. (Left) Unit cell of Ni_2MnGa in the $L2_1$ form. Thick solid lines highlight the $L1_0$ sub-shell as viewed from Mn and Ga XAFS. (Right) Tetrahedral cage of Mn and Ga surrounding Ni within the $L1_0$ sub-shell.

Jahn-Teller effect leading to increase of DOS at Fermi-level. Displacement of constituent atoms with varying amplitudes in the martensitic phase gives rise to dimpling of atomic planes and eventually leads to modulated structures. Following this work, the same inference was drawn based on photoemission study carried out by Ye *et al.*[9].

Understanding the effect of disorder in spinel chalcogenides

Spinel chalcogenides are materials with a general formula of AB_2X_4 (where X = S, Se, Te) that crystallize into a cubic form with space group Fd3m. The X anions form a cubic close-packed lattice, while A cations occupy the resultant tetrahedral sites and B cations occupy the octahedral sites. Amongst the various combinations of cations at the A and B sites, the ones with B = Cr have lately been receiving a lot of attention. Interesting functional properties like colossal magneto-capacitance and relaxor ferroelectricity have been reported for $CdCr_2S_4$, $HgCr_2S_4$ (refs 21–23) and $CdCr_2Se_4$ (ref. 24). Further, $CdCr_2S_4$ also exhibits colossal electro-capacitive, electroresistive, and magnetoresistive effects[25]. However, it is cautioned that slight lattice distortions and cation valence/site disorder can be detrimental to its properties. For example, the dielectric relaxation dynamics and origin of multiferroicity in $CdCr_2S_4$ initially received a critical scrutiny[26–30]. It was argued that the reason for fascinating properties displayed by the single crystal $CdCr_2S_4$ may lie in the defects and embedded impurities like halogen (Br, Cl) vapours on the crystal surface during the growth process, though, such arguments were countered with complimentary measurements confirming multiferroicity. Nonetheless, disorder and local distortions are believed to play an important role in determining the properties of this class of materials. For example, relaxor dipole in $CdCr_2S_4$ originates from the dynamic off-centering of Cr 3d ions as shown through pair distribution function analysis of X-ray powder diffraction data[31].

Background

Motivated with the complexity of multiferroicity and to isolate the role of local lattice distortions, we have created controlled disorder in $CdCr_2Se_4$ and studied its effect on the properties of interest. The disorder was created at two sites, first by substituting a small percentage of Se ions with isovalent S to obtain two compositions, $CdCr_2Se_{3.8}S_{0.2}$ and $CdCr_2Se_{3.6}S_{0.4}$ (ref. 32) and second by replacing up to 10% of Cd^{2+} ions with M = Sb^{3+}, In^{3+} and Sn^{4+} in $Cd_{1-x}M_xCr_2Se_4$ (ref. 33). The low percentage of substitutions was chosen so that the crystal structure is maintained, yet the role of disorder is sufficiently unravelled. The local crystal structure of such disordered series of compounds was contrasted with that of the parent composition, $CdCr_2Se_4$, using room temperature XAFS measurements and complimented by temperature-dependent Raman spectroscopy measurements.

Polycrystalline samples of desired compositions were prepared by conventional solid-state synthesis method. High purity (99.99%) starting elements were taken in stoichiometric ratios and ground to fine powder using mortar and pestle, in a glove box with controlled nitrogen gas atmosphere. The ground powder was pressed into pellets and sealed in evacuated quartz ampoules under the pressure of 10^{-5} mbar. These sealed ampoules were heated at a very slow rate to 923 K in a muffle furnace and held there for 48 h before cooling to room temperature. Repeated cycles of re-annealing were required to ensure the formation of phase pure compositions. These were characterized by powder XRD, EDX-SEM, four-probe resistivity, and d.c. magnetization recorded as a function of temperature as well as applied magnetic fields[32–34].

Results and discussion

Substitution of Cd^{2+} by a fair amount of M = Sb^{3+}, In^{3+}, Sn^{4+} in $Cd_{1-x}M_xCr_2Se_4$ can primarily be expected to bring about two changes: lattice distortions due to different atomic sizes of the substituents, and electronic charge redistribution amongst the cations. Thus the possibility of formation of spin clusters and structural phase transitions at low temperature cannot be overseen. Hence, we first studied the magnetic ordering of the prepared samples and found ferromagnetic order, albeit decreasing value of T_C in comparison to $CdCr_2Se_4$, in all the studied compositions. M versus T plots for select compositions are shown in Figure 11.

Next, synchrotron-based high resolution XRD (HR–XRD) measurements were undertaken as a function of temperature to check for any structural instability that might develop in the low temperature magnetically ordered state. These measurements were carried out at the Indian beamline at Photon-Factory, KEK, Japan. We did not observe any change in the XRD patterns down to 50 K, thus ruling out the possibility of any structural transitions. XRD patterns for Sb-substituted compositions are shown at Figure 12.

Having confirmed the stability of the structure, we carried out some quantitative analysis of the powder XRD data for the $Cd_{1-x}M_xCr_2Se_4$ (M = Sb^{3+}, In^{3+}, Sn^{4+}) compositions and our findings, as summarized in Figure 13, motivated us to implore the local crystal structure of these compositions, especially the Sn-substituted ones.

Here, the magnetic ordering temperature and the total moment were found to vary in a correlated fashion with the lattice constant of the respective compositions. It may be noted that the magnetic ground state of $CdCr_2Se_4$ is deeply related with its crystal structure and results from

competing Cr–Se–Cr FM and Cr–Cr AFM interactions. Local crystal structure of $Cd_{1-x}M_xCr_2Se_4$ was hence explored using Cr K-edge EXAFS. Measurement in transmission mode was carried out at room temperature using the RIGAKU R-XAS laboratory spectrometer, a facility established at IIT Indore. This spectrometer is equipped with a 3 kW X-ray source and Ge(111)
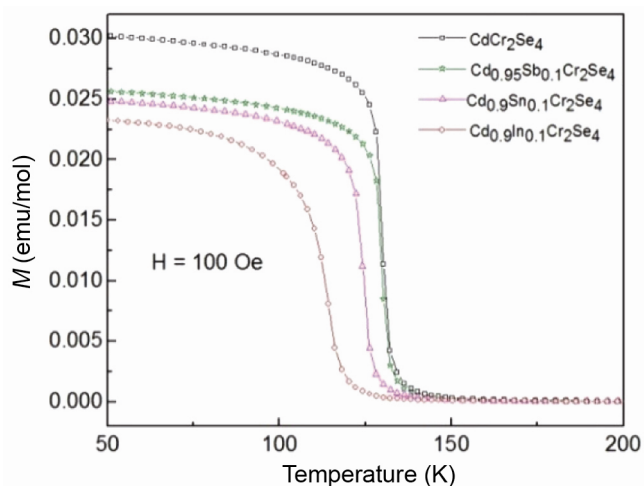
monochromator. The incident and transmitted intensities were measured using gas-filled ionization chamber and scintillation detector respectively. The absorber thickness was adjusted to restrict the absorption edge jump to an optimum value. The edge energy was calibrated using a Cr metal and Cr_2O_3 as standards.

Cr ions being located at octahedral site surrounded by Se ions, these ions are primary contributors to Cr K-edge XAFS. The Cd–Se bond distance and the corresponding thermal mean square factor (σ^2) were varied until a good fit was obtained in the range of 1–3 Å in the R-space and 2–10 Å^{-1} in the k-space. The magnitude and real
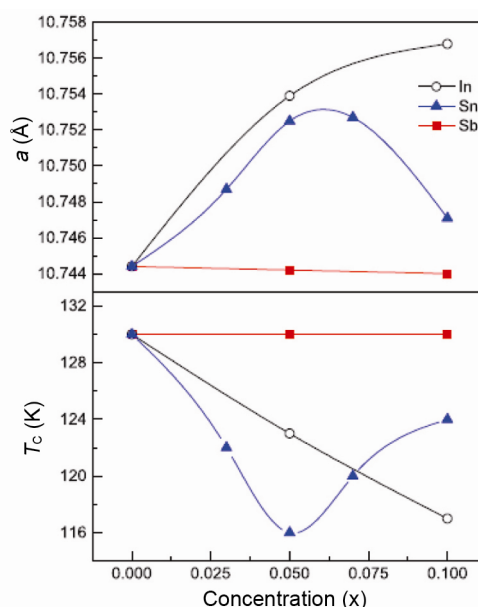

Figure 11. Magnetization as a function of temperature for $Cd_{0.9}M_{0.1}Cr_2Se_4$, with $M = Sb^{3+}$, In^{3+} and Sn^{4+}.
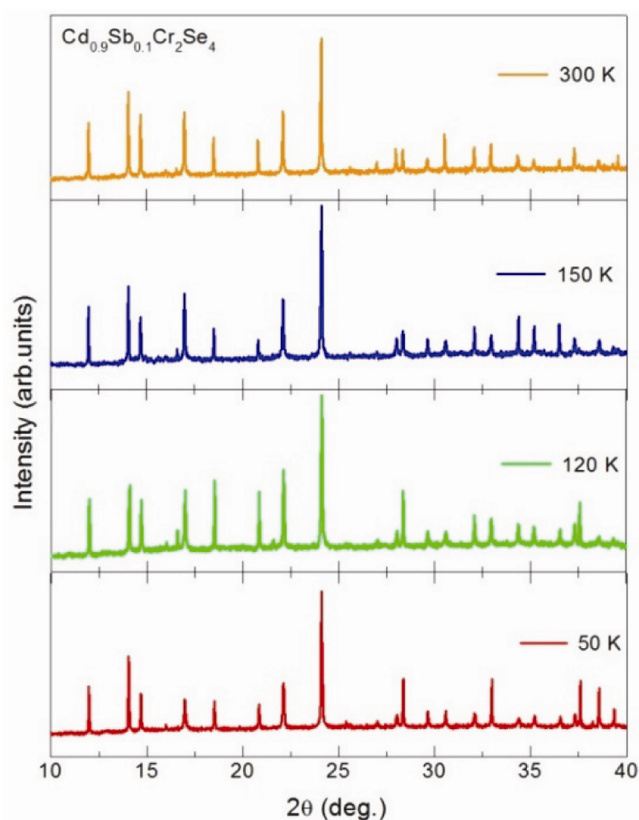
Figure 12. High-resolution synchrotron powder XRD patterns recorded across T_C of $Cd_{0.9}Sb_{0.1}Cr_2Se_4$.

Figure 13. Correlated changes in the lattice constants and magnetic ordering temperature of $Cd_{1-x}M_xCr_2Se_4$ compounds as a function of concentration x.

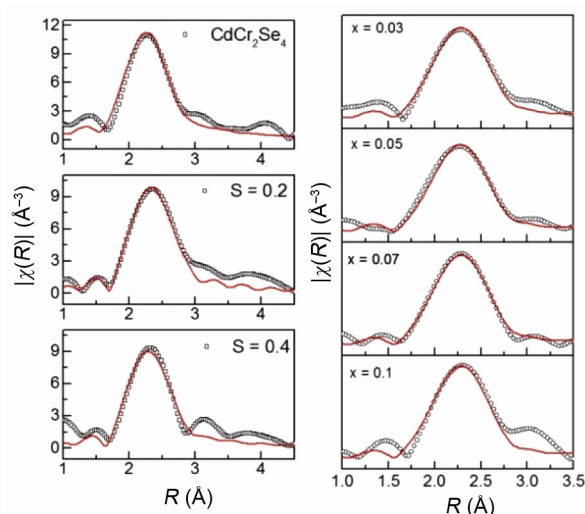**Figure 14.** Fitting to the magnitude and real component of FT Cr K-edge EXAFS spectra in $CdCr_2Se_4$, $CdCr_2Se_{4-x}S_x$ and $Cd_{1-x}Sn_xCr_2Se_4$.

components of FT are shown in Figure 14. Evidently, the fit for the parent composition is quite satisfactory, and the refined parameters for Cr–Se interaction are presented in Table 1.

Analysis of Sn-substituted compositions shows some striking anomalies in its local crystal structure. First, the bond distances obtained from XAFS show considerable deviation from those calculated from the XRD profile. Secondly, as can be seen from Figure 15, there is not much variation amongst the Cr–Se bond-lengths with changing Sn-concentration. But the second correlation comprising other Cr ions show considerable changes. This is particularly interesting because the Sn-substituted samples are affected by both lattice and charge effects as Sn^{4+} ion (0.55 Å) is much smaller than Cd^{2+} ions (0.78 Å).

We turn our attention to the other series, i.e. isovalent S-substitution at Se-site to obtain two compositions, $CdCr_2Se_{3.8}S_{0.2}$ and $CdCr_2Se_{3.6}S_{0.4}$. Having carried out all characterizations similar to the $Cd_{1-x}M_xCr_2Se_4$ series, EXAFS investigation was carried out for the S-substituted compositions. Similar data-fitting strategy was adopted for the two S-substituted compositions, albeit inclusion of S in the octahedral cage of anions and the fits are shown in Figure 14. The resultant Cr–Se/S bond distances and

σ^2 are listed in Table 1. We obtain unequal bond distances for Cr–Se and Cr–S, indicating structural distortion of the Cr octahedra at a local level within the overall cubic unit cell. As S^{2-} has a smaller ionic radius (1.84 Å) in comparison to Se^{2-} (1.98 Å), such an unequal bond distance is not surprising.

The question that arises is, to what extent does these local static distortions seen in the S and Sn substituted compositions impact the functional properties of

Table 1. Results of the fits to the room-temperature Cr K-edge data of $CdCr_2Se_{4-x}S_x$, and $Cd_{1-x}Sn_xCr_2Se_4$ R refers to the Cr–Se/Cr–S bond-length and σ^2 is the thermal mean-square variation in the bond length

Cr–Se/Cr–S	R (Å)	σ^2
$CdCr_2Se_4$	2.615(9)	0.00528(1)
Sn = 0.03	2.622(8)	0.0077(9)
Sn = 0.05	2.624(9)	0.00940(1)
Sn = 0.07	2.624(8)	0.00840(2)
Sn = 0.1	2.624(9)	0.00889(1)
S = 0.2	2.669(8)	0.0054(3)
	2.431(9)	0.0040(6)
S = 0.4	2.654(7)	0.0062(2)
	2.395(9)	0.0004(1)

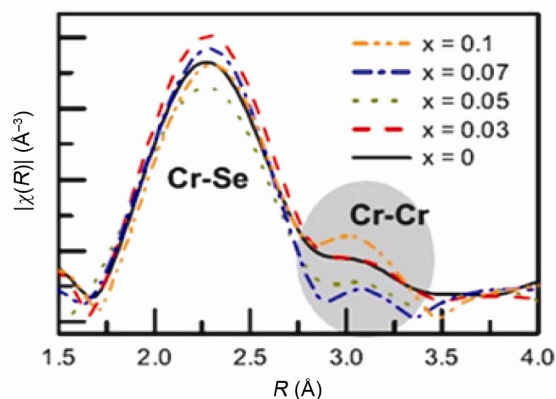**Figure 15.** Comparison of Cr–Se bond distance for different Sn concentrations of $Cd_{1-x}Sn_xCr_2Se_4$.
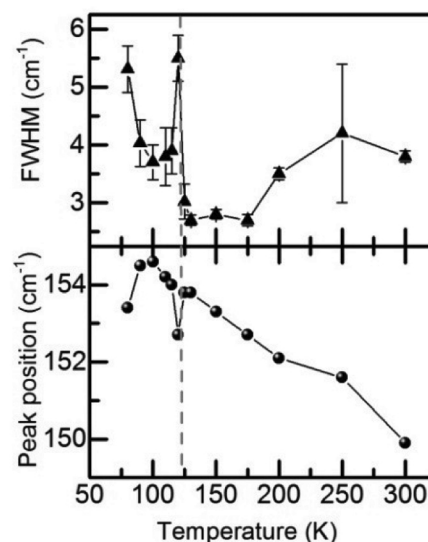

Figure 16. Temperature variation in the peak position of E_g mode and its FWHM in $CdCr_2Se_{4-x}S_x$ as obtained from Raman spectroscopy. Solid line represents straightline connecting the data points.
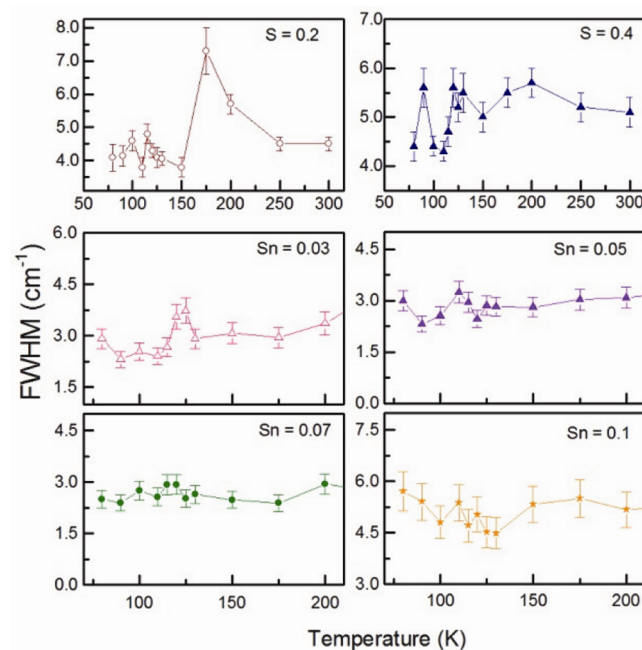

Figure 17. Temperature variation in the FWHM for E_g mode in the S- and Sn–doped $CdCr_2Se_4$ compositions. Considerable weakening of spin–phonon signature is seen in Sn-doped compositions as compared to S-doped.

CdCr$_2$Se$_4$ in particular, and spinel chalcogenides in general. Measurement of magnetic properties indicates only slight decrease in the ordering temperature for S-substituted compositions. The Sn-substituted compositions not only show change in T_C, the total magnetic moment also changes dramatically. It is found that Sn substitution brings about a charge imbalance at Cr-site creating a mixed valence Cr$^{2+/3+}$ state that manifests itself in the magnetic properties of the Sn-based samples. Another prominent effect of disorder is seen on the spin–phonon coupling present in the CdCr$_2$Se$_4$. The signature of spin–phonon coupling is the anomaly in temperature dependence of position and full-width–half-maximum (FWHM) of certain peaks associated with Cr–Se vibrational modes in Raman spectra. As seen in Figure 16, the parent composition exhibits spin–phonon coupling at its magnetic ordering temperature. Such a coupling is crucial for the much envisaged multiferroicity in CdCr$_2$Se$_4$.

This spin–phonon signature occurs prominently for CdCr$_2$Se$_{3.8}$S$_{0.2}$, and to some extent in CdCr$_2$Se$_{3.6}$S$_{0.4}$, as well. Overall, the coupling weakens due to increase in scattering of phonons brought about by the difference in atomic masses of Se and S ions. However, the Sn-substituted samples show a complete absence of such coupling. This is evident from the temperature dependent FWHM of the Raman modes shown in Figure 17. Thus, it is concluded that disorder indeed affects the magneto-structural coupling of these materials. If the distortions are limited to structural changes alone, a higher percentage of disorder is tolerable for materials properties. However, if the disorder causes charge-imbalance in addition to structural distortions, the effect is quite drastic[32–34].

Summary and perspectives

Combination of thermopower measurements and XAFS has been demonstrated to provide valuable insight into the crystal structure–electronic property correlation in technologically relevant materials like shape memory alloy, and multiferroics. Thermopower measurement provides valuable insight into the changes taking place in the DOS of the material of interest, which can serve as a preamble to electronic structure study using more advanced technique like photoemission spectroscopy. XAFS provide the essential local crystal structure information not accessible by the most common technique of X-ray diffraction.

As for the development of high ZT thermoelectric materials, high production costs and limited scalability do seem like an impediment in the large-scale industrial application of thermoelectric materials. Moreover, the quest for new materials, though generic, is advancing at a rapid rate with innovations being made on various aspects of materials synthesis techniques. But improvement in design optimization and efforts to reduce parasitic losses

in device fabrication are not able to keep pace with it. For now, however, is the time for careful studies of laboratory scale materials and to build up the knowledge base that will someday provide the fundamental insights for future use and hopefully address the issues of sustainable energy that we all face today.

1. Goldsmid, J. H., *Introduction to Thermoelectricity*, Springer Series in Material Science, 2010, vol. 121.
2. Altenkirch, E., Elektrothermische Kalteerzeugung und reversible elektrische Heizung. *Phys. Z.*, 1911, **12**, 920.
3. Koningsberger, D. C. and Prins, R. (eds), X-ray absorption: principles, applications, techniques of EXAFS, SEXAFS and XANES, Wiley-Interscience, 1988.
4. Rehr, J. J, Stern, E. A., Martin, R. L. and Davidson, E. R., Extended X-ray-absorption fine-structure amplitudes – wave function relaxation and chemical effects. *Phys. Rev. B*, 1978, **17**, 560.
5. Ashley, C. A. and Doniach, S., Theory of extended X-ray absorption edge fine structure (EXAFS) in crystalline solids. *Phys. Rev. B*, 1975, **11**(4), 1279.
6. Priolkar, K. R., Bhobe, P. A., Dias, S. S. and Paudel, R., Resistivity and thermopower of Ni$_{2.19}$Mn$_{0.81}$Ga alloy. *Phys. Rev. B*, 2004, **70**, 132408.
7. Bhobe, P. A., Monteiro, J. H., Cascalheira, J. C., Menditta, S. K., Priolkar, K. R. and Sarode, P. R., Composition and temperature dependence of the thermoelectric power of Ni$_{2+x}$Mn$_{1-x}$Ga alloys. *J. Phys.: Condens. Matter.*, 2006, **18**, 10843.
8. Bhobe, P. A., Priolkar, K. R. and Sarode, P. R., Local atomic structure of martensitic Ni$_{2+x}$Mn$_{1-x}$Ga: an EXAFS study. *Phys. Rev. B*, 2006, **74**, 224425.
9. Ye, M. *et al.*, Role of electronic structure in martensitic phase transition of Ni$_2$Mn$_{1+x}$Sn$_{1-x}$ studied by hard-X-ray photoelectron spectroscopy and *ab initio* calculation. *Phys. Rev. Lett.*, 2010, **104**, 176401.
10. D'Souza, S. W. *et al.*, Coexistence of charge–density wave and ferromagnetism in Ni$_2$MnGa. *Phys. Rev. B*, 2012, **85**, 085123.
11. Bhobe, P. A., Priolkar, K. R. and Sarode, P. R., Factors influencing martensitic transformation in Ni$_{50}$Mn$_{35}$Sn$_{15}$: an EXAFS study. *J. Phys.: Condens. Matter.*, 2008, **20**, 015219.
12. Bhobe, P. A., Priolkar, K. R. and Sarode, P. R., Local atomic arrangement and martensitic transformation in Ni$_{50}$Mn$_{35}$In$_{15}$: an EXAFS study. *J. Phys. D: Appl. Phys.*, 2008, **41**, 0450004.
13. Priolkar, K. R., Bhobe, P. A. and Sarode, P. R., Hybridization effects in Ni–Mn based shape memory alloys: XAFS study. *Adv. Mater. Res.*, 2008, **52**, 155.
14. Webster, P. J., Ziebeck, K. R. A., Town, S. L. and Peak, M. S., Magnetic order and phase transformation in Ni$_2$MnGa. *Philos. Mag.*, 1984, **49**, 295.
15. Brown, P. J., Crangle, J., Kanomata, T., Matsumoto, M., Neumann, K.-U., Ouladdiaf, B. and Ziebeck, K. R., The crystal structure and phase transitions of the magnetic shape memory compound Ni$_2$MnGa. *J. Phys.: Condens. Matter.*, 2002, **14**, 10159.
16. Vasil'ev, A. N. *et al.*, Structural and magnetic phase transitions in shape-memory alloys Ni$_{2+x}$Mn$_{1-x}$Ga. *Phys. Rev. B*, 1999, **59**, 1113.
17. Kübler, J., Williams, A. R. and Sommers, C. B., Formation and coupling of magnetic moments in Heusler alloys. *Phys. Rev. B*, 1983, **28**, 1745.
18. Martynov, V. V. and Kokorin, V. V., The crystal structure of thermally – and stress-induced martensites in Ni$_2$MnGa single crystals. *J. Phys. III France*, 1992, **2**, 739.
19. Zayak, A. T., Entel, P., Rabe, K. M., Adeagbo, W. A. and Acet, M., Anomalous vibrational effects in nonmagnetic and magnetic Heusler alloys. *Phys. Rev. B*, 2005, **72**, 054113.

20. Khovailo, V. V., Takagi, T., Bozhko, A. D., Matsumoto, M., Tani, J and Shavrov, V. G., Premartensitic transition in $Ni_{2+x}Mn_{1-x}Ga$ Heusler alloys. *J. Phys.: Condens. Matter.*, 2001, **13**, 9655.

21. Hemberger, J., Lunkenheimer, P., Fichtl, R., Krug von Nidda, H. A., Tsurkan, V. and Loidl, A., Relaxor ferroelectricity and colossal magnetocapacitive coupling in ferromagnetic $CdCr_2S_4$. *Nature*, 2005, **434**, 364.

22. Lunkenheimer, P., Fichtl, R., Hemberger, J., Tsurkan, V. and Loidl, A., Relaxation dynamics and colossal magnetocapacitive effect in $CdCr_2S_4$, *Phys. Rev. B*, 2005, **72**, 060103(R).

23. Weber, S., Lunkenheimer, P., Fichtl, R., Hemberger, J., Tsurkan, V. and Loidl, A., Colossal magnetocapacitance and colossal magnetoresistance in $HgCr_2S_4$. *Phys. Rev. Lett.*, 2006, **96**, 157202.

24. Hemberger, J., Lunkenheimer, P., Fichtl, R., Weber, S., Tsurkan, V. and Loidl, A., Multiferroic behaviour in $CrCr_2X_4$ ($X = S$, Se), *Physica B*, 2006, **378**, 363.

25. Sun, C. P. *et al.*, Colossal electroresistance and colossal magnetoresistance in spinel multiferroic $CdCr_2S_4$. *Appl. Phys. Lett.*, 2010, **96**, 122109.

26. Catalan Gustau, and Scott James F., Magnetoelectrics: is $CdCr_2S_4$ a multiferroicrelaxor? *Nature*, 2007, **448**, E4–E5.

27. Hemberger, J., Lunkenheimer, P., Fichtl, R., Krug von Nidda, H. A., Tsurkan, V. and Loidl, A., Magnetoelectrics: is $CdCr_2S_4$ a multiferroicrelaxor? (reply). *Nature*, 2007, **448**, E5–E6.

28. Catalan, G., Magnetocapacitance without magnetoelectric coupling. *Appl. Phys. Lett.*, 2006, **88**, 102902.

29. Scott, J. F., Electrical characterization of magnetoelectrical materials. *J. Mater. Res.*, 2007, **22**, 2053.

30. Pintilie, L. and Alexe, M., Ferroelectric-like hysteresis loop in nonferroelectric systems. *Appl. Phys. Lett.*, 2005, **87**, 112903.

31. Oliveira, G. N. P. *et al.*, Dynamic off-centering of Cr^{3+} ions and short-range magneto-electric clusters in $CdCr_2S_4$. *Phys. Rev. B*, 2012, **86**, 224418.

32. Behera, P., Suchismita and Bhobe, P. A., Crystal structure and magnetic property correlation in $Cd_{1-x}M_xCr_2Se_4$ (M = Sb, Sn, In), *J. Magn. Magn. Mater.*, 2015, **394**, 200.

33. Behera, P., Suchismita, Bhobe, P. A., Sathe, V. G. and Nigam, A. K., Local lattice distortions and magnetic properties of $CdCr_2Se_{4-x}S_x$. *J. Appl. Phys.*, 2016, **120**, 045107.

34. Behera, P., Suchismita, Bhobe, P. A., Sathe, V. G. and Nigam, A. K., Effect of disorder on spin–phonon coupling of $Cd_{1-x}Sn_xCr_2Se_4$ for ($0 < x < 0.1$), under review, 2017.